

Article

Design of TiO₂-Surfactin Hybrid Systems with Multifunctional Properties

Simona Ortelli ^{1,*}, Maurizio Vespignani ^{1,2}, Ilaria Zanoni ¹, Magda Blosi ¹, Claudia Vineis ³,
Andreana Piancastelli ¹, Giovanni Baldi ⁴, Valentina Dami ⁴, Stefania Albonetti ^{1,2,*} and Anna Luisa Costa ¹

- ¹ CNR-ISSMC (Former ISTEC), National Research Council of Italy-Institute of Science, Technology and Sustainability for Ceramics, Via Granarolo 64, 48018 Faenza, Italy
² Department of Industrial Chemistry “Toso Montanari”, Bologna University, Viale Risorgimento 4, 40136 Bologna, Italy
³ CNR-STIIMA, Institute of Intelligent Industrial Technologies and Systems for Advanced Manufacturing–Italian National Research Council, Corso Pella 16, 13900 Biella, Italy
⁴ Ce.Ri.Col, Colorobbia Consulting S.R.L., 50059 Sovigliana-Vinci, Italy
* Correspondence: simona.ortelli@istec.cnr.it (S.O.); stefania.albonetti@unibo.it (S.A.)

Abstract: In recent years, multifunctional inorganic–organic hybrid materials have been widely investigated in order to determine their potential synergetic, antagonist, or independent effects in terms of reactivity. The aim of this study was to design and characterize a new hybrid material by coupling well-known photocatalytic TiO₂ nanoparticles with sodium surfactin (SS), a biosurfactant showing high binding affinity for metal cations as well as the ability to interact with and disrupt microorganisms’ cell membranes. We used both chemical and colloidal synthesis methodologies and investigated how different TiO₂:SS weight ratios affected colloidal, physicochemical, and functional properties. We discovered a clear breaking point between TiO₂ and SS single-component trends and identified different ranges of applicability by considering different functional properties such as photocatalytic, heavy metal sorption capacity, and antibacterial properties. At low SS contents, the photocatalytic properties of TiO₂ are preserved (conversion of organic dye = 99% after 40 min), and the hybrid system can be used in advanced oxidation processes, taking advantage of the additional antimicrobial SS properties. At high SS contents, the TiO₂ photoactivity is inhibited, and the hybrid can be usefully exploited as a UV blocker in cosmetics, avoiding undesired oxidative effects (UV adsorption in the range between 300–400 nm). Around the breaking point (TiO₂:SS 1:1), the hybrid material preserves the high surface area of TiO₂ (specific surface area around 180 m²/g) and demonstrates NO_x depletion of up to 100% in 80 min, together with improved adhesion of hybrid antibacterial coating. The last design demonstrated the best results for the concurrent removal of inorganic, organic, and biological pollutants in water/soil remediation applications.

Keywords: hybrid system; nano-TiO₂; sodium surfactin; photocatalyst; sorption capacity; antibacterial coating



check for updates

Citation: Ortelli, S.; Vespignani, M.; Zanoni, I.; Blosi, M.; Vineis, C.; Piancastelli, A.; Baldi, G.; Dami, V.; Albonetti, S.; Costa, A.L. Design of TiO₂-Surfactin Hybrid Systems with Multifunctional Properties. *Molecules* **2023**, *28*, 1863. <https://doi.org/10.3390/molecules28041863>

Academic Editor: Juan Matos Lale

Received: 9 December 2022

Revised: 26 January 2023

Accepted: 13 February 2023

Published: 16 February 2023



Copyright: © 2023 by the authors. Licensee MDPI, Basel, Switzerland. This article is an open access article distributed under the terms and conditions of the Creative Commons Attribution (CC BY) license (<https://creativecommons.org/licenses/by/4.0/>).

1. Introduction

Sustainable wastewater management has become the primary agenda of the sustainable development goals worldwide [1].

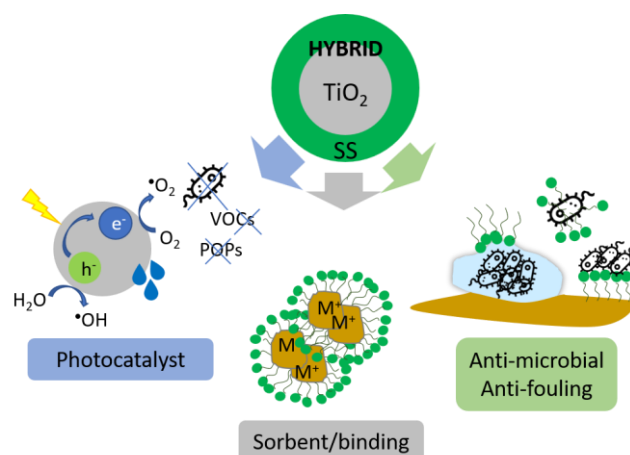
This challenge is addressed by technologies that promote a concurrent removal of organic (molecules, oils, microorganisms, etc.) and metal pollutants from contaminated sites (water or soil).

Nano-TiO₂ offers low cost, high reactivity, and easy recovery of photocatalytic technology. Its light-activated capacity to oxidate/mineralize organic compounds is of great relevance and significance in advanced oxidation processes for water and air depollution [2–5]. The possibility of activation in the visible light region as a result of metal and

nonmetal doping and the fabrication of composites has recently attracted increasing attention due to possible applications under outdoor solar or indoor LED-visible sources of irradiation. The design of TiO₂ nanoparticles (NPs) strongly affects their efficiency. It is influenced by: (1) quantum size effects such as band gap energy and the light-induced charge transfer between the adsorbate molecules and the substrate; (2) surface area effects such as the light absorption efficiency and the consequent surface photocarrier concentration; and (3) carrier diffusion effects such as the recombination rate of photogenerated carriers [1].

Microbial polymers are biosurfactants whose use is attracting increasing interest for the removal of metal(loid)s from soil, effluents, and wastewaters [2,3]. Surfactin, a cyclic lipopeptide produced by *Bacillus subtilis*, is considered one of the most effective biosurfactants [6]. Its low critical micelle concentration; high binding affinity for metal cations; foaming, emulsifying, and dispersing properties; high surface activity; and ability to interact and disrupt microorganisms' cell membranes make surfactin an ideal candidate for water/soil bioremediation and antibacterial/antiviral applications [7–13]. Surfactin also exhibits good stabilizing properties used in the sol–gel synthesis of metal nanoparticles. [14–16]. Thus, we decided to exploit the coupling between the two phases in order to investigate the physicochemical identity of the mix phase and the possible synergetic, antagonist, or independent effects in terms of functionality [17,18].

New inorganic–organic multicomponent materials based on TiO₂ and sodium surfactin (SS) biosurfactant were produced, characterized, and tested for their multifunction activity, as reported in Scheme 1.



Scheme 1. Multifunctional platform designed for the removal of water/soil pollutants.

Two synthesis design strategies, namely chemical sol–gel synthesis of TiO₂ nanoparticles (NPs) nucleated over SS solution and colloidal heterocoagulation, exploiting the attraction between opposite charge TiO₂ NPs and SS, were used to produce hybrid materials made by TiO₂.

We tested the photocatalytic activity vs. the degradation of rhodamine B (RhB) in water, the abatement of NO_x at gas phase, the sorption of Cu²⁺ ions, selected as probe metal, and the biocidal action following the ASTM E2149 procedure against Gram-positive bacteria *Staphylococcus aureus*.

2. Results and Discussion

2.1. Sol–Gel Synthesis (TiO₂@SS_S)

Data from colloidal characterization of TiO₂@SS_S samples, differing for the TiO₂:SS weight ratio (details in Section 3.2.1), are reported in Table 1. We observed an increase in hydrodynamic diameters, determined by DLS analysis (Figure S1 and Table 1), as a function of the SS amount. This was justified by the increase in the steric hindrance of the SS shell and by the destabilization of colloidal dispersion, which were caused by free, non-adsorbing molecules in solution (depletion flocculation) [19]. The zeta-potential curves as a function

of pH, reported in Figure 1, show an abrupt change in colloidal properties, passing from a 1:1 to 1:2 TiO₂:SS ratio. Two populations are clustered around the curves of the two separate components: one with nanometric hydrodynamic diameters, positive zeta potential, and an isoelectric point comparable with that of the TiO₂ reference sample (TiO₂@TX) and the other with micrometric hydrodynamic diameters, negative zeta potential, and an isoelectric point similar that of SS. This result offered a clear indication of which design option to select if we wish to prioritize the TiO₂ or the SS colloidal identity in the hybrid system.

Table 1. Data from colloidal characterization of TiO₂@SS_S samples obtained via sol–gel synthesis.

Sample	d _{DLS} (nm)	Zeta-pot _{ELS} (mV)	pH _{iep}
SS	nd *	−38 ± 6	1.7
TiO ₂ @TX	64 ± 2	+39 ± 7	6.2
TiO ₂ @SS_1:0.1_S	77 ± 4	+33 ± 6	6.1
TiO ₂ @SS_1:0.5_S	215 ± 15	+28 ± 5	6.0
TiO ₂ @SS_1:1_S	720 ± 143	+24 ± 4	6.0
TiO ₂ @SS_1:2_S	870 ± 84	−7 ± 2	1.7
TiO ₂ @SS_1:6_S	1000 ± 25	−40 ± 8	2.1
TiO ₂ @SS_1:8_S	1020 ± 178	−43 ± 5	1.7

nd *, not determined.

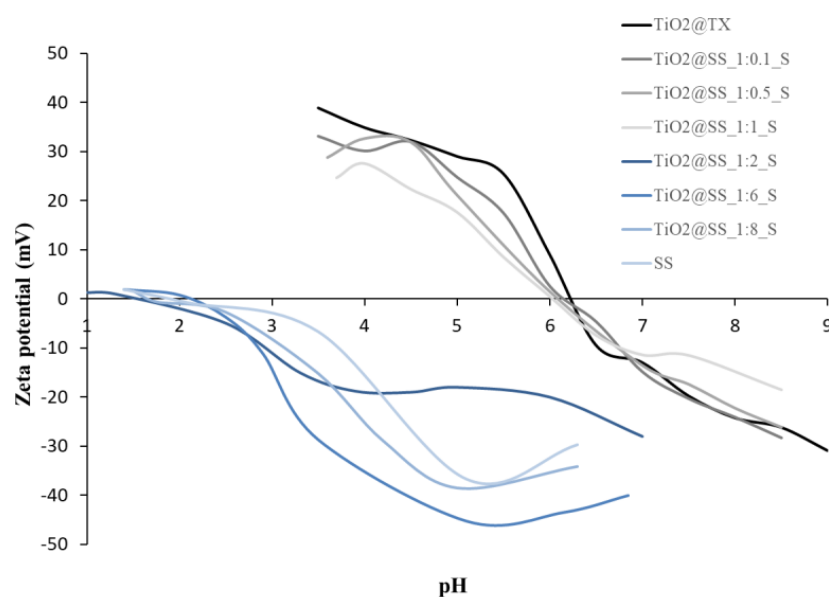


Figure 1. Zeta potential as a function of pH curves for TiO₂@SS_S samples obtained via sol–gel synthesis.

A breaking point, passing from the 1: 1 and 1: 2 TiO₂:SS ratios, was also observed in the XRD diffractograms (Figure 2). The peaks of TiO₂ anatase with small traces of brookite were observed up to the TiO₂:SS 1:1 weight ratio. In the group of samples with higher SS content, the characteristic peaks of the anatase phase disappeared. In this case, we can hypothesize the formation of very small clusters where the ionic phase is still in equilibrium with the solid [20,21] or the presence of amorphous titania phase [22]. In this group of samples, in relation to the high content of SS, we noticed the formation of NaCl as a by-product of the synthesis. This was identifiable based on peaks at $2\theta = 32^\circ$ and 47° . At $2\theta = 18^\circ$, a broad peak, which was attributable to the organic phase, confirmed the presence of the high concentration of SS.

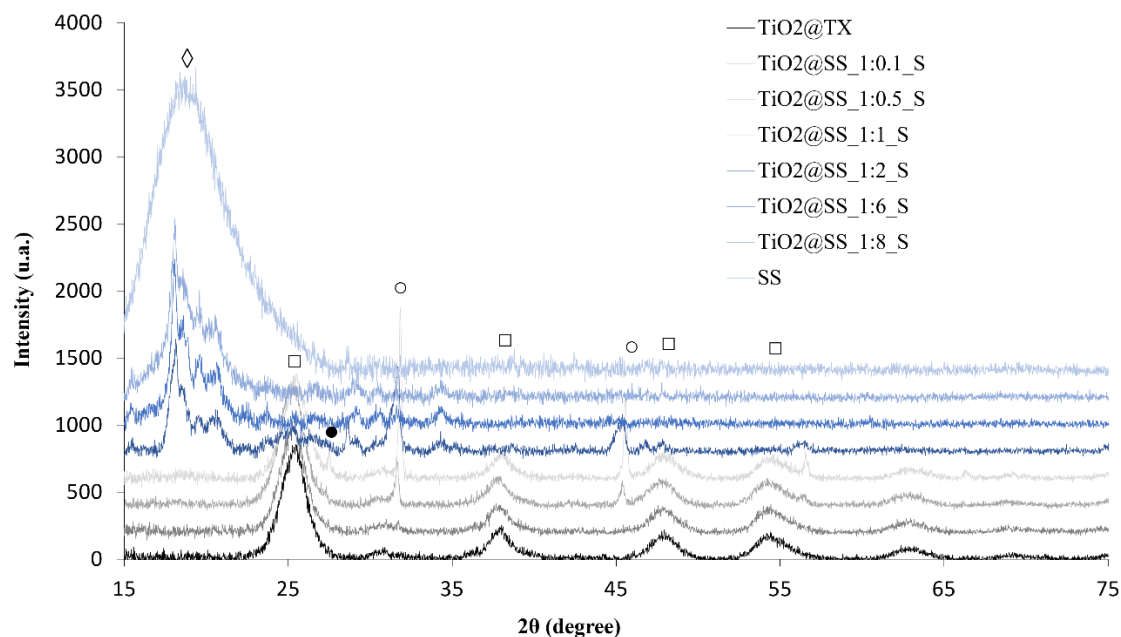


Figure 2. XRD diffractograms of $\text{TiO}_2@SS_S_SFD$ samples (\diamond , sodium surfactin; \square , anatase; \bullet , brookite; \circ , sodium chloride).

In order to verify the formation of TiO_2 NPs, TEM analysis was carried out. Figure 3 reports the TEM images of $\text{TiO}_2@SS_S_1:0.1$ and $\text{TiO}_2@SS_S_1:1$ sample, confirming the presence of crystalline well-dispersed TiO_2 NPs, with sizes ranging from 3 to 12 nm and from 2 to 10 nm, respectively. The selected area electron diffraction (SAED) pattern and the relative rotational average (Figure S2) showed that all rings can be indexed as a mixture of anatase (majority phase) and brookite nanocrystals, confirming the data obtained via XRD analysis (Figure 2). By increasing the content of SS in $\text{TiO}_2@SS_S_1:2$ and $\text{TiO}_2@SS_S_1:6$ samples, no evidence of the presence of TiO_2 NPs could be found via TEM analysis. Moreover, no evidence of the presence of crystalline NPs could be detected by SAED patterns. The TEM results confirm the hypothesis that very small clusters in equilibrium with their ionic phase should form at a high SS concentration, as the presence of SS hindered the growth of the as-formed nuclei.

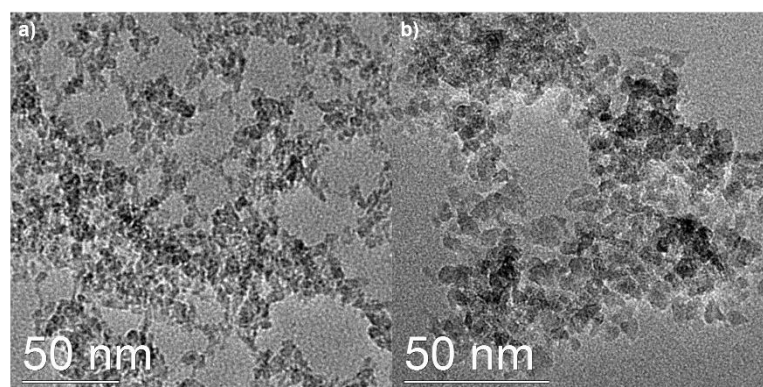


Figure 3. TEM images of (a) $\text{TiO}_2@SS_S_1:0.1$ and (b) $\text{TiO}_2@SS_S_1:1$ samples.

2.2. Heterocoagulation Process (TiO_2/SS_E)

The physical mixing of oppositely charged $\text{TiO}_2@TX_S$ and SS (Table 2) provided the heterocoagulated samples TiO_2/SS_E , whose components are mainly bound by electrostatic attractive interactions [23]. The samples were prepared at different $\text{TiO}_2:SS$ weight ratios (see Section 3.2.2 for details). Additionally, in this case, we investigated the colloidal behav-

ior of DLS and zeta-potential measurements and noted an increase in the hydrodynamic size of the multicomponent system with the increase in SS content. In particular, the sample corresponding to the TiO₂:SS 1:1 weight ratio was the first to reverse the positive zeta potential of TiO₂, which had dramatic consequences for the colloidal stability (DLS size around 1 μm), as reported in Table 2 and Figure S3a. With higher content of SS, the hydrodynamic diameter decreased, and the negative zeta potential of the composite increased due to the electrosteric contribution of S which, in the case of heterocoagulated samples, acts as a dispersing agent. As was the case for sol–gel samples, the isoelectric points (pH_{iep}) of the heterocoagulated samples at high content of SS (1:6 and 1:8 TiO₂:SS weight ratio) are coincident to that of SS (Figure S3b) even if the breaking point is not so evident, as in the previous case.

Table 2. Data from colloidal characterization of TiO₂/SS_E samples obtained via heterocoagulation.

Sample	d _{DLS} (nm)	Zeta-pot _{ELS} (mV)	pH _{iep}
SS	nd *	−38 ± 6	1.7
TiO ₂ @TX	64 ± 2	+39 ± 7	6.2
TiO ₂ /SS_1:1_E	1100 ± 200	−16 ± 4	3.4
TiO ₂ /SS_1:6_E	216 ± 5	−31 ± 58	1.7
TiO ₂ /SS_1:8_E	243 ± 2	−41 ± 5	1.5

nd *, not determined.

The XRD diffractograms showed the presence of both phases, as expected (Figure 4). TiO₂ (anatase phase) was recognized from characteristic peaks at $2\theta = 25^\circ, 38, 48,$ and 54° . Additionally, small traces of brookite were detected at $2\theta = 26^\circ$. The SS organic phase showed a broad peak at $2\theta = 18^\circ$. We observed a proportional increase in intensity of the SS peak as the SS content in the samples increased; this passed from TiO₂/SS_1:1_E to TiO₂/SS_1:8_E. The formation of a synthesis by-product, NaCl, was also identifiable, with peaks at $2\theta = 32^\circ$ and 47° .

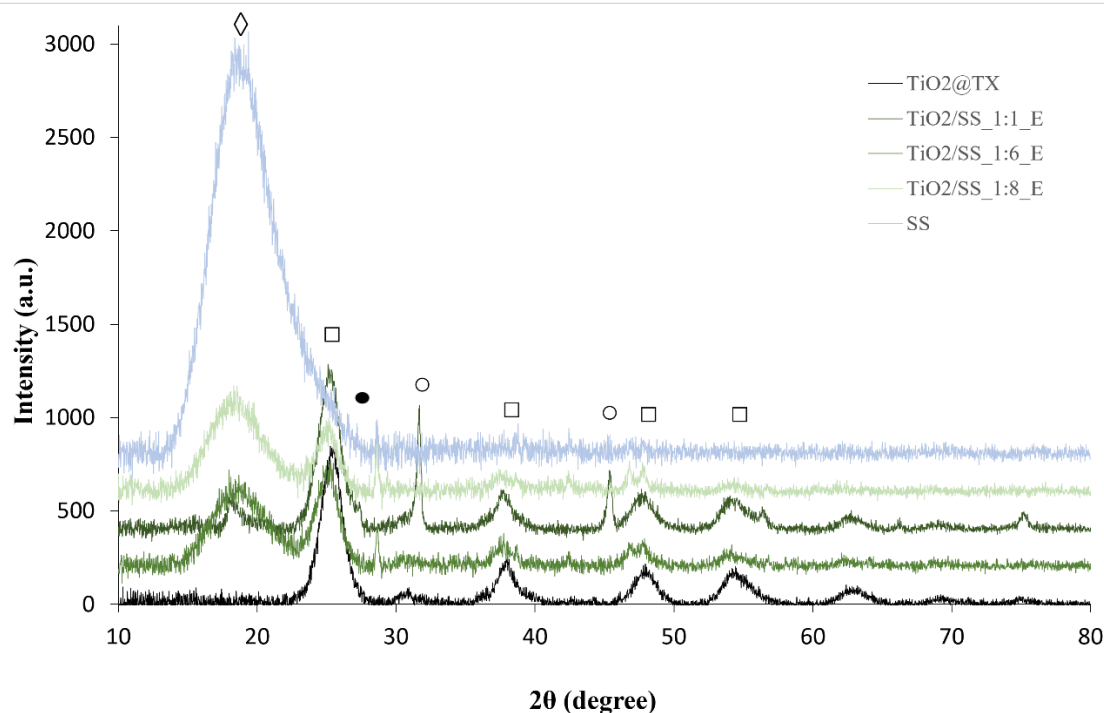


Figure 4. XRD diffractograms of TiO₂/SS_E_SFD samples (◇, sodium surfactin; □, anatase; ●, brookite; ○, sodium chloride).

2.3. Comparison between $\text{TiO}_2@SS_{1:1_S}$ and $\text{TiO}_2/SS_{1:1_E}$

The $\text{TiO}_2@SS_{1:1_S}$ and $\text{TiO}_2/SS_{1:1_E}$ samples are the most representative for both synthesis methods of hybrid systems; in fact, they represent the breaking point, with a shift of properties from TiO_2 to the SS component. Therefore, these samples were further investigated by additional characterization techniques (FTIR spectroscopy and BET analysis).

In Figure 5a, comparison between the FTIR spectra of $\text{TiO}_2@SS_{1:1_S}$ and $\text{TiO}_2/SS_{1:1_E}$ samples with single components ($\text{TiO}_2@TX$ and SS) is reported. The reference $\text{TiO}_2@TX$ (black curve) showed a broad band at $500\text{--}800\text{ cm}^{-1}$ corresponding to the vibration of Ti-O-O bond [24] and Ti-O stretching [25], confirming the presence of TiO_2 . Moreover, we observed some peaks in the wavenumber range $1100\text{--}1600\text{ cm}^{-1}$; these are attributable to Triton X. Their low intensity is due to the high TiO_2 :Triton X weight ratio (Table S1). The peaks at 1100 and 1243 cm^{-1} correspond to the asymmetric stretch of aromatic ether; those in the range $1360\text{--}1450\text{ cm}^{-1}$ are related to the C-H bending vibration; and peaks at 1511 and 1610 cm^{-1} correspond to the stretching vibration of the benzene group [26]. The light-blue curve in Figure 5a shows the FTIR spectrum of the SS component, which clearly highlights the typical peaks of lipopeptide biosurfactant, with peaks at 3350 and 1528 cm^{-1} attributed to NH-stretching mode and peaks at $2956\text{--}2870\text{ cm}^{-1}$ and $1467\text{--}1368\text{ cm}^{-1}$ representative of the C-H group of aliphatic chains ($-\text{CH}_3$; $-\text{CH}_2-$) with symmetric stretching at 2870 cm^{-1} .

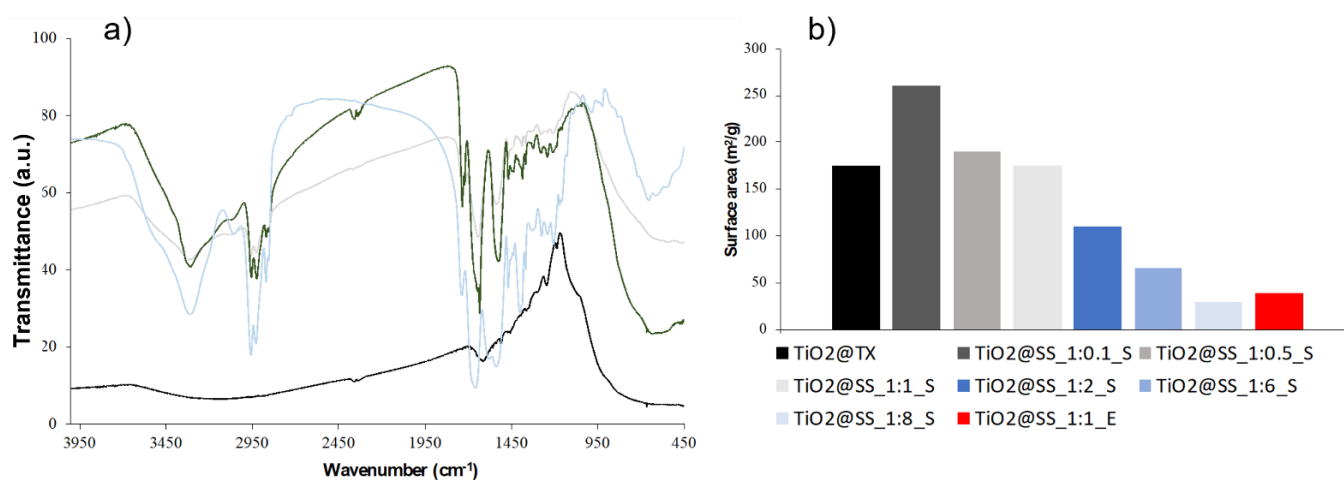


Figure 5. (a) FTIR spectra of $\text{TiO}_2@TX$ (black), SS (light blue), $\text{TiO}_2@SS_{1:1_S}$ (light gray), and $\text{TiO}_2/SS_{1:1_E}$ (dark green) samples and (b) specific surface area data (m^2/g).

The FTIR analysis on hybrid $\text{TiO}_2@SS_{1:1_S}$ and $\text{TiO}_2/SS_{1:1_E}$ samples allowed us to confirm the presence of typical functional groups of both TiO_2 and SS. The main characteristic peaks of TiO_2 and SS were observed in both $\text{TiO}_2@SS_{1:1_S}$ and $\text{TiO}_2/SS_{1:1_E}$ samples (Figure 5a). Through detailed comparison of the two samples, we can observe a lower intensity of peaks corresponding to the SS and the absence of characteristic bands of SS at high wavenumber in the $\text{TiO}_2@SS_{1:1_S}$ sample (blue curve). On the other hand, in the $\text{TiO}_2/SS_{1:1_E}$ sample (dark-green curve), obtained by heterocoagulation, all characteristic peaks of SS were recognized. These observations could be justified by a stronger interaction between TiO_2 NPs and SS in the sample obtained by sol-gel synthesis method, with the formation of a new hybrid phase slightly different from the single component.

The specific surface areas (SSAs) of spray-freeze-dried (SFD) powders are reported in Figure 5b. Samples synthesized using a sol-gel method at a low SS concentration show high values of surface area comparable with that of the TiO_2 component. The SSA of $\text{TiO}_2:SS_{1:1_S}$ sample is five-fold higher than the corresponding heterocoagulated sample. This result is most likely due to intimate molecular interaction between the two components in the sol-gel-synthesized samples, which promotes a real dispersing action of SS over TiO_2 NPs. The abrupt decrease in surface area that occurs as a result of the increasing

TiO₂:SS weight ratio is in agreement with the increased agglomeration caused by the SS depletion action discussed previously (Table 1). Additionally, the low surface area of the heterocoagulated sample is justified by the high degree of agglomeration of this sample, which decreases the number of TiO₂-accessible surface sites.

2.4. Functional Characterization

2.4.1. Photocatalytic Tests

The results of photocatalytic tests performed in water and expressed as a percentage of conversion of the rhodamine B (RhB) under visible solar light are reported in Figure S4 and Table 3.

Table 3. Conversion (%) and kinetic constant (min^{−1}) obtained by photocatalytic tests of TiO₂@SS_S samples synthesized via the sol–gel method.

Sample	Conversion (%)	k (min ^{−1})
TiO ₂ @TX (ref.)	99	9.5×10^{-2}
TiO ₂ @SS_1:0.1_S	99	8.5×10^{-2}
TiO ₂ @SS_1:0.5_S	90	4.0×10^{-2}
TiO ₂ @SS_1:1_S	87	2.3×10^{-2}
TiO ₂ @SS_1:2_S	47	0.6×10^{-2}
TiO ₂ @SS_1:6_S	16	0.5×10^{-2}
TiO ₂ @SS_1:8_S	12	0.1×10^{-2}

Firstly, no samples demonstrated adsorption of RhB after one hour of contact in the dark (Figure S4a). The TiO₂@TX reference component had the highest photocatalytic performance, with a conversion of 99% and the highest kinetic constant (9.5×10^{-2} min^{−1}). The hybrid systems for low SS content showed very good photocatalytic performance, with conversion around 90% and a high kinetic constant (k) up to the sample with TiO₂:SS 1:0.5. Increasing the content of SS led to an abrupt decrease in photocatalytic activity up to samples TiO₂@SS_1:6_S and TiO₂@SS_1:8_S, which did not demonstrate any significant photocatalytic activity despite the photoactivation (absorption in the range between 300–400 nm, reported in Figure S8 and Table S3). The reduction in photocatalytic activity around TiO₂:SS 1:0.5 and 1:1 weight ratios is in agreement with the abrupt change in physicochemical properties and the previously noted absence of TiO₂ crystalline peaks detectable through XRD (Figure 2) or TEM SAED analysis. Moreover, the trend caused by the increased amount of SS surrounding TiO₂ NPs can be justified by the shielding effect of organic SS coating, which depresses the photocatalytic activity of TiO₂ NPs [27].

The results of tests performed using samples prepared via heterocoagulation (TiO₂/SS_E) are reported in Figure S5 and Table 4.

Table 4. Conversion (%) and kinetic constant (min^{−1}) obtained via photocatalytic tests of TiO₂/SS_E samples prepared via heterocoagulation.

Sample	Conversion (%)	k (min ^{−1})
TiO ₂ @TX (ref.)	99	9.5×10^{-2}
TiO ₂ /SS_1:1_E	18	0.5×10^{-2}
TiO ₂ /SS_1:6_E	5	0.6×10^{-3}
TiO ₂ /SS_1:8_E	5	0.6×10^{-3}

For samples obtained via heterocoagulation, almost no sorbent capacity was observed for RhB after one hour of contact in darkness (Figure S5a). The samples obtained via heterocoagulation had very poor photocatalytic performance, with conversion data of less than 20% and a very low kinetic constant. As expected, the presence of the SS layer surrounding TiO₂ NPs, which depresses the specific surface area (Figure 5b), also has a strong shielding

effect on the TiO₂ photocatalytic performances, with a reasonable quenching of radicals produced by TiO₂ NPs due to their organic coating [28].

Overall, the comparison of photocatalytic performances of TiO₂@SS_1:1_S and TiO₂/SS_1:1_E samples highlights how, in the sol–gel-synthesized hybrids specifically, it is possible to take advantage of the highly surface-area-dependent photocatalytic properties of TiO₂.

2.4.2. Sorption Tests

The results of sorption tests performed on representative samples are reported in Table 5. They are expressed as the Cu²⁺ sorption capacity, which allows it to simulate these materials' use for the removal of heavy metals from wastewater. The data show similar trends for both sol–gel synthesis and heterocoagulation samples, with a sorption capacity that is dependent on the SS content. Below the TiO₂:SS 1:1 weight ratio, the samples show the same sorption capacity of TiO₂, whilst at the highest concentration of SS, the samples show the same behavior of SS alone. This result suggests the main sorption/complexing role of SS is solely dependent on the amount of SS available and not its degree of agglomeration or interaction with the TiO₂ component. Moreover, we observed no significant increase in Cu²⁺ sorption over time, demonstrating that the sorption ability of all these samples is characterized by fast kinetics.

Table 5. Results of Cu²⁺ sorption (mgCu²⁺/g_{sample}) tests performed on representative samples.

Sample	Cu ²⁺ Sorption (mg Cu ²⁺ /g _{sample})	
	1 h	24 h
SS	2.53	2.53
TiO ₂ @TX (ref.)	1.36	1.39
TiO ₂ @SS_1:0.1_S	1.16	1.28
TiO ₂ @SS_1:1_S	1.28	1.23
TiO ₂ @SS_1:8_S	2.53	2.53
TiO ₂ /SS_1:1_E	1.18	1.35
TiO ₂ /SS_1:8_E	2.53	2.53

2.4.3. Antibacterial Tests

Biocidal action was tested on TiO₂@SS_S nanosols obtained via sol–gel synthesis and de-positated on polyester textile substrates via a dip-pad curing method [29]. In Table 6, the add-on (%) and the bacterial reduction (%) data are reported.

Table 6. Results of antibacterial tests performed on representative samples.

Sample	Add-on (%)	Bacterial Reduction (%)
SS	1.7	40
TiO ₂ @TX (ref.)	3.1	72
TiO ₂ @SS_1:0.1_S	3.9	89
TiO ₂ @SS_1:1_S	3.9	85
TiO ₂ @SS_1:8_S	5.3	77

The SS alone showed a low bacterial reduction (40%) due to the low add-on value (1.7%). The presence of TiO₂ increases the amount of material that can be transferred on the sample, with consequent improvement of antibacterial properties (up to 89% for the TiO₂@SS_1:0.1_S sample). We also observed a decrease in performance at the highest SS content despite the highest add-on, confirming that the SSA and availability of free surface sites also play a huge role in the biological reactivity in this case. Overall, it was difficult to determine if synergic effects occurred between the two potentially active components; the only evident effect is the improved adhesion (add-on value) provided by the TiO₂ phase.

2.4.4. NO_x Abatement Tests

Photocatalytic performances were also evaluated on TiO₂@SS_S coated textiles through NO_x abatement tests. The data expressed as NO depletion trend as a function of time are reported in Figure 6.

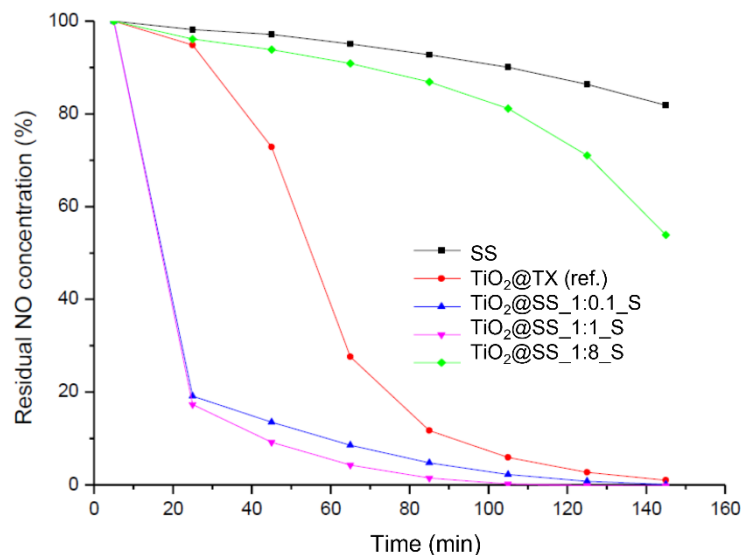


Figure 6. NO depletion trend as a function of UV light time of irradiation.

As expected, the inactivity of SS alone was demonstrated by the negligible depletion of NO (SS—black curve). In agreement with this result, low reactivity was also found at the highest SS concentration (TiO₂@SS_S_1:8—green curve) despite the highest amount of composite deposited on the textile (add-on value reported in Table 6). On the other hand, the reference (TiO₂@TX) and the hybrid samples with low SS content showed complete NO depletion after 2h of UV light exposure. This trend concurs with the results of photocatalytic and antibacterial tests reported in Sections 2.4.1 and 2.4.3, respectively. As expected, at a high concentration of TiO₂, the photocatalytic properties of the inorganic photocatalyst prevail, with consequent high NO depletion. The higher degradation kinetics of hybrid samples compared with reference TiO₂ (depletion around 80% for TiO₂:SS_1:0.1 and 1:1_ and <5% for TiO₂@TX, at 20 min) is highly encouraging and can be justified by the dispersing capability of SS, which maximizes the availability of TiO₂ active surface sites. (See Supplementary Materials)

3. Materials and Methods

3.1. Materials

Titanium(IV) isopropoxide, hydrochloric acid, Triton X, rhodamine B and copper chloride were purchased by Merck Life Science S.r.l. (Milano, Italy). Sodium surfactin was provided by AmbrosiaLab (Ferrara, Italy). All the reagents were used without further purification.

3.2. Methods

The hybrid materials based on TiO₂ and sodium surfactin (SS) biosurfactant were prepared using two synthesis design strategies: sol–gel synthesis and heterocoagulation.

3.2.1. Sol–Gel Synthesis (TiO₂@SS_S)

TiO₂ nanoparticles nucleated over SS solution were obtained via classical sol–gel synthesis via acidic catalysis starting from titanium(IV) isopropoxide, replacing the chemical surfactant (Triton X) at a very low concentration in the synthesis process (TiO₂:Triton X 1:0.06—TiO₂@TX_S) with the bio-surfactant SS [30]. The TiO₂ nanosuspensions (TiO₂@SS_S) were prepared with varying TiO₂:SS weight ratios (1:0.1; 1:0.5; 1:1; 1:2; 1:6 and 1:8). The

sol-gel-synthesis processes are schematized in Figure S6a. All the samples prepared by sol-gel-synthesis process are summarized in Table S1.

3.2.2. Heterocoagulation Process (TiO₂/SS_E)

The product TiO₂@TX_S was mixed with aqueous solution of SS in a pH range in which both surfaces TiO₂@TX and SS had opposite charges to promote the electrostatic interaction. The heterocoagulated samples were prepared with varying TiO₂:SS weight ratios (1:1; 1:6, and 1:8) and maintained under stirring for 24 h to favor electrostatic interaction. The heterocoagulation process is schematized in Figure S6b. All the samples prepared via heterocoagulation are listed in Table S2.

3.2.3. Spray-Freeze-Drying Technique

The spray-freeze-drying technique (Figure S7) was employed here to obtain handy powders (SFD), starting from the TiO₂- and SS-based nanosuspensions prepared by both methods (sol-gel-synthesis and heterocoagulation process) by means of a lab-scale granulator instrument, LS-2 (PowderPro, Mölnådal, Sweden). The nanosuspensions were atomized through a peristaltic pump, blowing nitrogen gas at 0.4 bar through a 100 µm nozzle, and nebulized into a stirred solution of liquid nitrogen to enable instantaneous freezing of each generated drop. The so-frozen drops were placed into a freeze-drying apparatus with a pressure of 0.15 mbar and a temperature of −1 °C to promote the sublimation process, which was completed within 48 h, and a highly porous granulated powder was produced. All the samples prepared via the SFD process are summarized in Tables S1 and S2.

3.3. Physicochemical Characterizations

3.3.1. Colloidal Characterization

The particle size distribution and zeta potential were determined at 25 °C using a Zetasizer Nanoseries (Malvern Instruments, Malvern, UK) via dynamic light scattering (DLS) and electrophoretic light scattering (ELS) techniques, respectively. The DLS technique can calculate the hydrodynamic diameter of suspended particles, and the Smoluchowski equation was applied to convert the electrophoretic mobility to zeta potential. After a 2 min temperature equilibration step, samples underwent three measurements; the hydrodynamic diameter and zeta potential were obtained by averaging these measurements. The instrument is equipped with an auto-titration unit, which enables the identification of the isoelectric point (pH_{IEP}) and automatically adds to the sample KOH 0.1 M or HCl 0.1 M in order to explore the zeta-potential trend within a selected pH range. The measurements were performed on the TiO₂- and SS-based nanosuspensions prepared via both methods (sol-gel synthesis and heterocoagulation) at 0.1 g L^{−1} concentration.

3.3.2. X-ray Diffraction (XRD)

XRD measurements were carried out on sample powders obtained using a spray-freeze-drying technique (SFD) at room temperature with a Bragg/Brentano diffractometer (X'pertPro PANalytical, Malvern Panalytical, Malvern, UK) equipped with a fast X'Celerator detector, using a Cu anode as the X-ray source (Kα, λ = 1.5418 Å). Diffractograms were recorded in the range 10–80° 2θ counting for 0.2 s every 0.05° 2θ step.

3.3.3. Transmission Electron Microscopy (TEM)

The transmission electron analyses on TiO₂@SS_S nanosols obtained via sol-gel synthesis were performed with a FEI TECNAI F20 microscope (FEI F20, Thermo Fisher Scientific, Waltham, MA, USA) operating at 200 keV. The instrument is also equipped with a dispersion micro-analysis of energy (EDS) (EDAX, Thermo Fisher Scientific, Waltham, MA, USA) and the scanning transmission electron microscopy (STEM) accessory (FEI F20, Thermo Fisher Scientific, Waltham, MA, USA). The TEM images were taken in the phase contrast mode and selected area electron diffraction (SAED). STEM pictures were recorded using a high-angle annular dark field (HAADF) detector: in this imaging mode, the intensity I

is proportional to $Z^{1.7}t$, where Z is the mean atomic number, and t is the thickness of the specimen. After 1:1000 dilution in water, the nanosols were sonicated for four minutes, then deposited on a holey carbon film supported by a gold grid, and dried at 100 °C.

3.3.4. Fourier Transform Infrared (FTIR) Spectroscopy

FTIR analysis was performed on the TiO₂@SS samples after the SFD process. The powders were pelletized with KBr, adding ca. 1.25 mg of powder to 100 mg of KBr. The measurements were obtained using a Nicolet iS5 spectrometer (Thermo Fisher Scientific Inc., Waltham, MA, USA). A wave number range between 400 and 4000 cm⁻¹ was set for the analysis, and 24 runs were performed for each measurement with a resolution of 1 cm⁻¹ using the IR accessory (model iD1). The positions of the peaks were identified by means of the OMNIC software (v9.2, Thermo Fisher Scientific, Waltham, MA, USA) and comparing values with the data in the literature.

3.3.5. Specific Surface Area by BET Method

Specific surface areas of spray-freeze-dried powders were measured by N₂ physisorption apparatus (Surfer Thermo Scientific) via Brunauer–Emmett–Teller (BET) (Surfer, Thermo Fisher Scientific, Waltham, MA, USA) analysis, in which samples were pre-treated under a vacuum at 200 °C for 1 h.

3.4. Functional Characterizations

3.4.1. Photocatalytic Degradation of Rhodamine B (RhB)

Photocatalytic degradation of RhB was conducted in a beaker at room temperature. The typical setup foresees the addition of samples, both in suspension and in powder (at 0.1 g L⁻¹ concentration), to 150 mL of a RhB aqueous solution. In order to establish an absorption/desorption equilibrium between catalyst and RhB, the solution was kept in the dark for about 60 min, which proved to be a suitable time to ensure the equilibrium. Absorption/desorption phenomena occurring during the stirring were verified and evaluated as negligible in relation to the overall photocatalytic reaction. The suspension was stirred and irradiated via a solar simulator (SUN 2000 11000 model, Abet Technologies, Milford, CT, USA) with 1000 W intensity. The lamp was switched on before the beginning of the photocatalytic test to stabilize the emission power. The analyses were performed using a quartz cuvette as a sample-holder. The degradation reaction progress was monitored at regular times (10, 20, 30, 40, 50, and 60 min) by withdrawing and centrifuging (7500 rpm for 10 min) 3 mL of solution and measuring the absorbance at 554 nm with a single-beam spectrophotometer (UV/Vis Hach Lange, DR 3900, Hach, Loveland, CO, USA). The photocatalytic activity was quantified as the photodegradation rate constant of catalyst k (min⁻¹). The photodegradation of RhB in presence of a catalyst can be considered a pseudo-first-order reaction and can be described by Equation (1):

$$\ln(C_0/C) = kt \quad (1)$$

According to the Lambert–Beer law, the absorbance is proportional to the RhB concentration, so $\ln(C_0/C)$ is calculated by measuring the initial concentration (C_0) and absorbance (A_0) and after a certain irradiation time t (A_t). The value of k was assessed by plotting $\ln(C_0/C)$ versus time (t). The conversion, calculated at $t = 120$ min, indicates the ratio between the amount of reagent consumed and the amount of reagent initially present in the reaction environment; this was determined by Formula (2):

$$\text{Conversion (\%)} = (A_0 - A_t)/A_0 \times 100 \quad (2)$$

3.4.2. Sorption Tests

The prepared samples, in powder form, were dispersed in water and kept in contact with a solution of CuCl₂ (10 mg L⁻¹) at room temperature. The tests were performed in the presence of 2.5 g L⁻¹ of adsorbent samples under stirring and at a working pH of

4.5. To quantify the sorption, after keeping the samples in contact with Cu^{2+} , 8 mL were centrifuged at 4500 rpm for 40 min by ultrafiltering the sample with centrifugal filter units (Polyethersulfone, Amicon filter 5 KDa, Millipore, Burlington, MA, USA). In this way, we separated the powder samples from the solution and quantified them via inductively coupled plasma atomic emission spectroscopy coupled with a OneNeb nebulizer (ICP-OES 5100—vertical dual view apparatus—Agilent Technologies, Santa Clara, CA, USA); the non-absorbed Cu^{2+} remained part of the solution despite the increase in time (1 and 24 h). The analyses were performed in radial viewing mode, and calibration curves were obtained with 0.1, 1.0, 10.0, and 100.0 mg L^{-1} standards for the element. Nitric acid was added to standards and diluted samples (1:10 v/v). The calibration curve was evaluated and showed a good correlation coefficient (R^2) above 0.99. Results from ICP-OES were reported as the average of three independent measurements with relative standard deviation.

3.4.3. Antibacterial Tests

Biocidal action was tested on $\text{TiO}_2@SS_S$ nanosols, obtained via sol-gel synthesis, which was deposited on polyester textile substrates via the dip-pad curing method. The textile was washed in an ultrasonic bath for 15 min in water and dried in an oven at 100 °C. Then, the washed textile was dipped in the $\text{TiO}_2@SS_S$ nanosols for 3 min, squeezed in two rolls to eliminate the excess of suspension (pad stage), dried in a stove at 80 °C, and finally cured at 120 °C for 10 min to fix the NPs to the fabric. A triple-layer impregnation was carried out, achieving the final dry add-on value (AO%; Equation (3)), which is defined as the percent amount of the finishing agent added to the fabric with respect to the initial weight of the latter; i.e.,

$$\text{AO}\% = [(w_f - w_i)/w_i] \times 100 \quad (3)$$

where w_i and w_f are the weights of the fabric before and after the dip-pad curing process.

The antibacterial tests were assessed following the ASTM E2149 procedure and addition of Gram-positive bacteria *Staphylococcus aureus* (*S. aureus*) ATCC 6538. Before the tests, the $\text{TiO}_2@SS_S$ coated polyester textiles were pre-irradiated for 2 h 30 min under UV light (Osram ULTRA-Vitalux lamp 300 W). The test culture was incubated in a nutrient broth for 24 h and then diluted to a concentration of $1.5\text{--}3.0 \times 10^5$ CFU mL^{-1} (working solution). Next, 1 g of each treated fabric was transferred to a flask containing 50 mL of the working solution. All flasks were shaken for 1 h at 190 rpm. After a series of dilutions, 1 ml of the solution was plated in nutrient agar. The inoculated plates were incubated at 37 °C for 24 h, and the surviving cells were counted. The biocidal action was expressed in percent bacteria reduction by counting the surviving cells after contact with the test specimen (A) compared to the number of bacterial cells in the working solution (B), according to Equation (4):

$$\text{Reduction}\% = [(A - B)/B] \times 100 \quad (4)$$

3.4.4. NO_x Abatement Test

The NO_x abatement test was conducted on $\text{TiO}_2@SS_S$ nanosol-coated textiles (10 × 10 cm), prepared via the dip-pad curing method (as described in the previous Section 3.4.3). The analyses were conducted under controlled conditions at a temperature of 26 ± 2 °C and a relative humidity of $44 \pm 4\%$ and under UV irradiation (Osram ULTRA Vitalux lamp 300 W) at an intensity of 50 W m^{-2} . The analyses were performed by injecting a pollutant gas consisting of dry air, moist air, and NO in the measuring system in the presence of the coated textiles. Then, the concentration of the gases (NO, NO_x , and NO_2) was monitored with a chemiluminescence detector (Thermo, model 42i, Thermo Fisher Scientific, Waltham, MA, USA). The NO degradation reaction progress was monitored at regular times (25, 45, 65, 85, 105, 125, and 145 min). The kinetics of the degradation reaction were obtained, plotting the NO depletion (%) as a function of time of activation.

4. Conclusions

Hybrid systems based on TiO₂ and sodium surfactin (SS) components were successfully synthesized via two different approaches (sol–gel synthesis and heterocoagulation). Physicochemical and colloidal properties characterization highlighted two main populations with distinct behavior. At the breaking point, around TiO₂:SS 1:1/1:2, the colloidal stability of the system abruptly decreased, with dramatic consequences for functional performances. On the contrary, the presence of surfactin at a low concentration improved the TiO₂ dispersibility, increasing the availability of active surface sites. This resulted in the highest performances in terms of photocatalytic degradation of RhB in water, abatement of NO in gas, and antibacterial properties against *Staphylococcus aureus* of coated textiles. In particular, the hybrid system with TiO₂:SS 1:1 preserved the high surface area of TiO₂ (specific surface area around 180 m²/g), caused a NO_x depletion up to 100% in 80 min, and improved adhesion of the hybrid antibacterial coating, suggesting that it is the best hybrid design for the concurrent removal of inorganic, organic, and biological pollutants in water/soil remediation applications. The evaluation of potential synergic effects of the hybrid systems leads us to the following conclusions: (1) at low SS contents, the photocatalytic properties of TiO₂ are preserved, and the hybrid systems can be used in advanced oxidation processes, taking advantage of the additional SS properties; (2) at high SS contents, TiO₂ loses its photoactivity due to the SS coating quenching effect, so the hybrid can be usefully exploited as a UV blocker in cosmetics, avoiding undesired oxidative effects; (3) in the combined adsorbent system, the TiO₂ can improve the stability and density of the biosurfactant, allowing easy transport and recovery from the medium. Overall, the eco-design of hybrid systems and the proven concurrent removal of inorganic, organic, and biological pollutants can be successfully exploited in environmental remediation technologies.

Supplementary Materials: The following supporting information can be downloaded at: <https://www.mdpi.com/article/10.3390/molecules28041863/s1>, Table S1: Sample code and TiO₂:SS weight ratio of nanosuspensions obtained by sol–gel-synthesis process and relative powders obtained by SFD process; Table S2: Sample code and TiO₂:SS weight ratio of nanosuspensions obtained by heterocoagulation process and relative powders obtained by SFD process; Table S3: Adsorption properties derived by UV-Vis. Analysis; Figure S1: Particle size distribution of TiO₂@SS samples obtained by sol–gel-synthesis method; Figure S2: SAED patterns of (a) TiO₂@SS_S_1:0.1 and (b) TiO₂@SS_S_1:1 sample; Figure S3: (a) Particle size distribution and (b) zeta potential as a function of pH curves of TiO₂/SS_E samples obtained by heterocoagulation process; Figure S4: (a) Trend of A/A₀ and (b) conversion (%) over time of TiO₂@SS_S samples obtained by sol–gel-synthesis method; Figure S5: (a) Trend of A/A₀ and (b) conversion (%) over time of TiO₂/SS_E samples obtained by heterocoagulation process; Figure S6: Scheme of (a) sol–gel processes using Triton X (TX) and sodium surfactin (SS) as surfactant and (b) heterocoagulation process; Figure S7: Schematization of the spray-freeze-drying process; Figure S8: Diffuse reflectance over different wavelengths of TiO₂@SS_S samples.

Author Contributions: Conceptualization, S.O., M.B. and A.L.C.; methodology, M.V., I.Z., A.P., G.B., V.D. and C.V.; investigation, M.V., I.Z., A.P. and C.V.; data curation, S.O., M.V. and I.Z.; writing—original draft preparation, S.O.; writing—review and editing, S.O., M.V., I.Z., M.B., S.A. and A.L.C.; supervision, S.A. and A.L.C.; funding acquisition, A.L.C. All authors have read and agreed to the published version of the manuscript.

Funding: This work was supported by the “ASINA” (Anticipating Safety Issues at the Design Stage of NANO Product Development) European project. ASINA has received funding from the European Union’s Horizon 2020 research and innovation programme under grant agreement No 862444. This paper reflects only the author’s view, and the Commission is not responsible for any use that may be made of the information it contains.

Institutional Review Board Statement: Not applicable.

Informed Consent Statement: Not applicable.

Data Availability Statement: The data presented in this study are available on request from the corresponding author. The data are not publicly available due to privacy restrictions.

Acknowledgments: The authors would like to thank Stefano Manfredini and AmbrosiaLab for providing free sodium surfactin samples.

Conflicts of Interest: The authors declare no conflict of interest.

Sample Availability: Samples of the compounds TiO₂@SS and TiO₂/SS are available from the authors.

References

1. Transforming Our World: The 2030 Agenda for Sustainable Development, United Nations. Available online: <https://sdgs.un.org/2030agenda> (accessed on 20 December 2022).
2. Lee, S.Y.; Park, S.J. TiO₂ Photocatalyst for Water Treatment Applications. *J. Ind. Eng. Chem.* **2013**, *19*, 1761–1769. [[CrossRef](#)]
3. Ortelli, S.; Blosi, M.; Delpivo, C.; Gardini, D.; Dondi, M.; Gualandi, I.; Tonelli, D.; Aina, V.; Fenoglio, I.; Gandhi, A.A.; et al. Multiple Approach to Test Nano TiO₂ Photo-Activity. *J. Photochem. Photobiol. A Chem.* **2014**, *292*, 26–33. [[CrossRef](#)]
4. Faccani, L.; Ortelli, S.; Blosi, M.; Costa, A.L. Ceramized Fabrics and Their Integration in a Semi-Pilot Plant for the Photodegradation of Water Pollutants. *Catalysts* **2021**, *11*, 1418. [[CrossRef](#)]
5. Koivisto, A.J.; Trabucco, S.; Ravegnani, F.; Calzolari, F.; Nicosia, A.; del Secco, B.; Altin, M.; Morabito, E.; Blosi, M.; Costa, A.; et al. Nanosized Titanium Dioxide Particle Emission Potential from a Commercial Indoor Air Purifier Photocatalytic Surface: A Case Study. *Open Res. Eur.* **2022**, *2*, 84. [[CrossRef](#)]
6. Eras-Muñoz, E.; Farré, A.; Sánchez, A.; Font, X.; Gea, T. Microbial Biosurfactants: A Review of Recent Environmental Applications. *Bioengineered* **2022**, *13*, 12365–12391. [[CrossRef](#)] [[PubMed](#)]
7. THE COVID DECADE Understanding the Long-Term Societal Impacts of COVID-19. Available online: <https://www.thebritishacademy.ac.uk/documents/3238/COVID-decade-understanding-long-term-societal-impacts-COVID-19.pdf> (accessed on 20 December 2022).
8. Théatre, A.; Cano-Prieto, C.; Bartolini, M.; Laurin, Y.; Deleu, M.; Niehren, J.; Fida, T.; Gerbinet, S.; Alanjary, M.; Medema, M.H.; et al. The Surfactin-Like Lipopeptides from *Bacillus* spp.: Natural Biodiversity and Synthetic Biology for a Broader Application Range. *Front. Bioeng. Biotechnol.* **2021**, *9*, 623701. [[CrossRef](#)] [[PubMed](#)]
9. Singh, A.; van Hamme, J.D.; Ward, O.P. Surfactants in Microbiology and Biotechnology: Part 2. Application Aspects. *Biotechnol. Adv.* **2007**, *25*, 99–121. [[CrossRef](#)]
10. Zezzi do Valle Gomes, M.; Nitschke, M. Evaluation of Rhamnolipid and Surfactin to Reduce the Adhesion and Remove Biofilms of Individual and Mixed Cultures of Food Pathogenic Bacteria. *Food Control* **2012**, *25*, 441–447. [[CrossRef](#)]
11. Moryl, M.; Spetana, M.; Dziubek, K.; Paraszkiwicz, K.; Rózsalska, S.; Płaza, G.A.; Rózsalski, A. Antimicrobial, Antiadhesive and Antibiofilm Potential of Lipopeptides Synthesised by *Bacillus subtilis*, on Uropathogenic Bacteria. *Acta Biochim. Pol.* **2015**, *62*, 725–732. [[CrossRef](#)]
12. Vollenbroich, D.; Vater, J.; Maria Kamp, R.; Pauli, G. Mechanism of Inactivation of Enveloped Viruses by the Biosurfactant Surfactin from *Bacillus subtilis*. *Biologicals* **1997**, *25*, 289–297. [[CrossRef](#)]
13. Kracht, M.; Rokos, H.; Ozel, M.; Kowall, M.; Pauli, G.; Vater, J. Antiviral and Hemolytic Activities of Surfactin Isoforms and Their Methyl Ester Derivatives. *J. Antibiot.* **1999**, *52*, 613–619. [[CrossRef](#)] [[PubMed](#)]
14. Satyanarayana Reddy, A.; Chen, C.Y.; Chen, C.C.; Jean, J.S.; Chen, H.R.; Tseng, M.J.; Fan, C.W.; Wang, J.C. Biological Synthesis of Gold and Silver Nanoparticles Mediated by the Bacteria *Bacillus subtilis*. *J. Nanosci. Nanotechnol.* **2010**, *10*, 6567–6574. [[CrossRef](#)] [[PubMed](#)]
15. Krishnan, N.; Velramar, B.; Pandiyan, R.; Velu, R.K. Anti-Pseudomonas and Anti-Endotoxic Effects of Surfactin-Stabilized Biogenic Silver Nanocubes Ameliorated Wound Repair in Streptozotocin-Induced Diabetic Mice. *Artif. Cells Nanomed. Biotechnol.* **2018**, *46*, 488–499. [[CrossRef](#)] [[PubMed](#)]
16. Singh, B.R.; Dwivedi, S.; Al-Khedhairi, A.A.; Musarrat, J. Synthesis of Stable Cadmium Sulfide Nanoparticles Using Surfactin Produced by *Bacillus Amyloliquifaciens* Strain KSU-109. *Colloids Surf. B Biointerfaces* **2011**, *85*, 207–213. [[CrossRef](#)] [[PubMed](#)]
17. Ortelli, S.; Costa, A.L.; Zaroni, I.; Blosi, M.; Geiss, O.; Bianchi, I.; Mehn, D.; Fumagalli, F.; Ceccone, G.; Guerrini, G.; et al. TiO₂@BSA Nano-Composites Investigated through Orthogonal Multi-Techniques Characterization Platform. *Colloids Surf. B Biointerfaces* **2021**, *207*, 112037. [[CrossRef](#)] [[PubMed](#)]
18. Blosi, M.; Briigliadori, A.; Zaroni, I.; Ortelli, S.; Albonetti, S.; Costa, A.L. Chlorella Vulgaris Meets TiO₂ NPs: Effective Sorbent/Photocatalytic Hybrid Materials for Water Treatment Application. *J. Environ. Manag.* **2022**, *304*, 114187. [[CrossRef](#)]
19. Jenkins, P.; Snowden, M. Depletion Flocculation in Colloidal Dispersions. *Adv. Colloid Interface Sci.* **1996**, *68*, 57–96. [[CrossRef](#)]
20. Monticone, S.; Tufeu, R.; Kanaev, A.V.; Scolan, E.; Sanchez, C. Quantum Size Effect in TiO₂ Nanoparticles: Does It Exist? *Appl. Surf. Sci.* **2000**, *162–163*, 565–570. [[CrossRef](#)]
21. Vorontsov, A.V.; Tsybulya, S.V. Influence of Nanoparticles Size on XRD Patterns for Small Monodisperse Nanoparticles of CuO and TiO₂ Anatase. *Ind. Eng. Chem. Res.* **2018**, *57*, 2526–2536. [[CrossRef](#)]
22. Hu, G.; Chen, S.; Shi, Q.; He, X.; Chen, P. Determination of the Amorphous Phase in Titania and Its Influence on Photocatalytic Properties. *Appl. Catal. B Environ.* **2016**, *195*, 39–47. [[CrossRef](#)]

23. Ortelli, S.; Costa, A.L. Nanoencapsulation Techniques as a “Safer by (Molecular) Design” Tool. *Nano-Struct. Nano-Objects* **2018**, *13*, 155–162. [[CrossRef](#)]
24. Rajakumar, G.; Rahuman, A.A.; Roopan, S.M.; Khanna, V.G.; Elango, G.; Kamaraj, C.; Zahir, A.A.; Velayutham, K. Fungus-Mediated Biosynthesis and Characterization of TiO₂ Nanoparticles and Their Activity against Pathogenic Bacteria. *Spectrochim. Acta A Mol. Biomol. Spectrosc.* **2012**, *91*, 23–29. [[CrossRef](#)] [[PubMed](#)]
25. Al-Amin, M.; Chandra Dey, S.; Rashid, T.U.; Ashaduzzaman, M.; Shamsuddin, S.M. Solar Assisted Photocatalytic Degradation of Reactive Azo Dyes in Presence of Anatase Titanium Dioxide. *Int. J. Latest Res. Eng. Technol.* **2016**, *2*, 14–21.
26. Rojas, J.A.; Ardila-Rodríguez, L.A.; Diniz, M.F.; Gonçalves, M.; Ribeiro, B.; Rezende, M.C. Optimization of Triton X-100 Removal and Ultrasound Probe Parameters in the Preparation of Multiwalled Carbon Nanotube Buckypaper. *Mater. Des.* **2019**, *166*, 107612. [[CrossRef](#)]
27. Costa, A.L.; Ortelli, S.; Blosi, M.; Albonetti, S.; Vaccari, A.; Dondi, M. TiO₂ Based Photocatalytic Coatings: From Nanostructure to Functional Properties. *Chem. Eng. J.* **2013**, *225*, 880–886. [[CrossRef](#)]
28. Ortelli, S.; Blosi, M.; Albonetti, S.; Vaccari, A.; Dondi, M.; Costa, A.L. TiO₂ based Nano-Photocatalysis Immobilized on Cellulose Substrates. *J. Photochem. Photobiol. A Chem.* **2014**, *276*, 58–64. [[CrossRef](#)]
29. Ortelli, S.; Costa, A.L.; Dondi, M. TiO₂ Nanosols Applied Directly on Textiles Using Different Purification Treatments. *Materials* **2015**, *8*, 7988–7996. [[CrossRef](#)]
30. Baldi, G.; Bitossi, M.; Barzanti, A. Method for the Preparation of Aqueous Dispersions of TiO₂ in the Form of Na-Noparticles, and Dispersions Obtainable with This Method. WO2007088151A1, 16 January 2013.

Disclaimer/Publisher’s Note: The statements, opinions and data contained in all publications are solely those of the individual author(s) and contributor(s) and not of MDPI and/or the editor(s). MDPI and/or the editor(s) disclaim responsibility for any injury to people or property resulting from any ideas, methods, instructions or products referred to in the content.